RSC Advances

PAPER

View Article Online
View Journal | View Issue

Cite this: *RSC Adv.*, 2020, **10**, 7898

Synthesis, characterization and photo-catalytic activity of guar-gum-*g*-aliginate@silver bionanocomposite material†

Imran Hasan, *[a] Rais Ahmad Khan, *[b] Walaa Alharbi,[c] Khadijah H. Alharbi,[d] Maymonah Abu Khanjer[b] and Ali Alslame [b]

Received 7th January 2020
Accepted 10th February 2020

DOI: 10.1039/d0ra00163e

rsc.li/rsc-advances

The green mechanism for the synthesis of nanoparticles and their application to the wastewater treatment is of inordinate curiosity to the research community. Herein we outline a novel method for the synthesis of silver nanoparticles *via* a green route using alginate-guar gum blend (GG-Alg@Ag) and their application to degrade methylene blue (MB) dye. The synthesized material was characterized by FTIR, XRD, SEM-EDX, TEM, TGA-DTG, AFM, and UV-vis techniques. A combination of RSM and CCD was employed to compute the system and optimized values of various interacting parameters such as exposure time (120 min), pH (4.98), dye concentration (194 mg L^{-1}), and catalyst dose (0.07 g) with a photodegradation capacity of 92.33% and desirability 1.0. The mechanism of degradation reaction was best elucidated by the pseudo-second-order model suggesting chemical deposition of MB on the GG-Alg@Ag surface through followed by the reduction mechanism in the occupancy of visible light. The optical studies indicated a value of 2.5 eV by Tauc's plot for bandgap energy (E_g) for GG-Alg@Ag bionanocomposite.

1. Introduction

Dyes belong to a group of unnatural organic materials and are frequently used in various textile industries.[1,2] Methylene blue (MB) is a water-soluble dye and used as a colorant in industries associated with the production of textile products. However, these dyestuffs are allegedly liable to liberate a large quantity of highly toxic colored pollutants that degrade water quality and cause several precarious and chronic disorders to animals and human beings, such as anaemia, bladder irritation, and gastrointestinal problems.[3–5] Intractable dyes containing extreme values of COD (>150 ppm), TOC (2900 mg L^{-1}), and BOD (>80 mg L^{-1}) have deteriorated aesthetic values in water resources.[6,7] Thus, based on high-level environmental challenges posed by MB, it has become essential to remove it from wastewater before its release into the natural environment. Extraction of MB from polluted water includes photodegradation, organic–inorganic ion exchange, electrodialysis, and chemical precipitation.[8–12] Among these, photodegradation is the most systematized method because of its ease in functionality and cost-effectiveness.[13–15]

Recently, silver nanoparticles have received considerable interest inferable from their broad scope of use in the field of bio-detection, catalysis, adsorption, and biotechnology.[16–18] Generally, a chemical coprecipitation method using reducing agents is employed for the growth of Ag nanoparticles, but excess use can create potential environmental and biological issues.[19,20] A green route for the synthesis of nanoparticles has been employed by various researchers because of its use of environmentally friendly solvents that provide better biocompatibility and stability to the nanoparticles.[21] With adequate biodegradability, surface functionality, and ecofriendly green processing, biopolymers such as starch,[22] alginate,[23] chitosan,[24] and cellulose[25,26] are widely utilized for the synthesis of nanoparticles owing to their biocompatibility and ecofriendly nature. They facilitate a controlled-size green environment for the growth of NPs through the formation of various types of physical and chemical bonds.[27,28]

The present study presents the eco-friendly green synthesis of Ag nanoparticles using a blend of guar gum and alginate as stabilizing and reducing agents. Alginate is generally considered as the crosslink mixture of linear α-(1,4) linked α-L-guluronate and β-D-mannuronate residues arranged in a non-regular, block-wise pattern along the linear chain while guar gum is the naturally occurring branched biopolymer β-D-mannopyranosyl units linked with single membered α-D-glucopyranosyl units as side branches.[28,29] Thus, the functionalization of Ag

[a]*Environmental Research Laboratory, Department of Chemistry, Chandigarh University, Gharuan, Mohali, Punjab, 140301, India. E-mail: imranhasan98@gmail.com*

[b]*Department of Chemistry, College of Science, King Saud University, Riyadh-11451, Kingdom of Saudi Arabia. E-mail: krais@ksu.edu.sa*

[c]*Department of Chemistry, Faculty of Science, King Khalid University, P.O. Box 9004, Abha, Kingdom of Saudi Arabia*

[d]*Department of Chemistry, Science and Arts College, Rabigh Campus, King Abdulaziz University, Jeddah, Kingdom of Saudi Arabia*

† Electronic supplementary information (ESI) available. See DOI: 10.1039/d0ra00163e

nanoparticles with GG-Alg blends provides a platform for better interactions and biocompatibility with biological agents and better affinity towards carcinogenic pollutants because of the availability of a surplus amount of surface –OH and –COOH groups.[30] The material was further explored for sunlight interceded photodegradation of MB from wastewater, and different parameters were optimized *via* response surface methodology (RSM). RSM is a collection of a few scientific and measurable procedures whose principle objective is to determine the ideal operational conditions for the process.[31,32] The utilization of RSM in an adsorption procedure can result in an improved adsorption limit, a diminished test fluctuation, a closer affirmation of yield reaction to the ostensible and target necessities, and a decreased advancement time.[33,34]

2. Materials and methods

2.1. Chemicals

Guar gum powder was purchased from Sigma Aldrich, India. Sodium alginate, $AgNO_3$, and Methylene blue were purchased from Merck India. The stock solution of Methylene blue was prepared by adding a precise amount of MB in deionized water.

2.2. Synthesis of GG-Alg@Ag bionanocomposite

A method of *in situ* green synthesis was utilized for the synthesis of a GG-Alg@Ag bionanocomposite by allowing for the growth of Ag nanoparticles (NPs) in the GG-Alg matrix.[35] To a 0.05 M $AgNO_3$ solution, 2% (w/v) alginate and 1% (w/v) guar gum solution were mixed at 303 K at a stirring rate of 12 000 rpm for 24 h. As the nucleation of Ag NPs with alginate moieties begins, the system turns into a pale yellow color, and further assessment of AgNPs was completed using an ultraviolet-visible light (UV-vis) spectrophotometer as shown in Fig. S1.†[36] For product formation, the mixture of GG-Alg/Ag was added dropwise from a glass syringe using 22-sized needle into 150 mL of a fluid calcium chloride solution blended at 400 rpm. The concentration of $CaCl_2$ in the solution increased from 3% to 5% w/v. Finally, the material was placed under a hot air oven to be completely dried for 5 h at 40 °C and preserved under vacuum conditions for further characterization and experimentation.

2.3. Analytical techniques used for characterization of sample

The type of functional groups and bonding in the material were analyzed using Fourier Transform Infrared spectroscopy, in particular, the PerkinElmer (PE1600, USA). A Rigaku Ultima IV X-ray diffractometer was utilized for the assessment of the solid structure of the bionanocomposite material. The surface morphological structure of the material was examined using scanning electron microscopy (SEM; JEOL GSM 6510LV, Japan). The samples wrapped in a gold film were prepared before their introduction to the SEM imaging cell. The molecule size and dissemination of nanoparticles in the polymer framework of the blended bionanocomposite were determined by utilizing a JEM 2100 (Japan) transmission electron microscope. The MB concentration in the supernatant was estimated using a UV-vis spectrophotometer (UV-1900, Shimadzu). The alteration of the arrangement pH was determined using an Elico Li 120 pH meter. INTEGRA (NT-MDT-INTEGRA) was used for the Atomic Force Microscopy (AFM) analysis. The thermal stability was determined by thermogravimetric analysis (TGA, PerkinElmer model, STA 6000) and thermal derivative analysis (DTG, PerkinElmer Pyris 6). The TGA thermograms were recorded for 20 mg of powder sample at a heating rate of 10 °C min^{-1} in the temperature range of 30–800 °C under the nitrogen atmosphere.

2.4. Design of experiments

The experimental design was constructed using Design Expert, and a CCD was utilized to run the experiments. The complete design consisted of four factors of exposure time ($X1$), pH ($X2$), initial MB concentration ($X3$), and catalyst dose ($X4$), each at five levels (-2, -1, 0, +1, +2) as listed in Table S1.† A quadratic regression model activated by the CCD was utilized for the prediction of photodegradation behavior of MB on GG-Alg@Ag for four variables as follows:[37]

$$y = b_0 + \sum_{i=1}^{n} b_i x_i + \sum_{i=1}^{n} b_{ii} {x_i}^2 + \sum_{1 \le i < j}^{n} b_{ij} x_i x_j + \varepsilon \quad (1)$$

where y is the response of the experimental design, model constant is b_0, the linear constant is b_i, the quadratic constant is b_{ii}, and interaction constant is b_{ij}. Parameters x_i and x_j correspond to independent variables of the design, n is the number of variables considered, and ε is the residual statistical term.

The MB concentration was analyzed by UV-vis spectrophotometer, and the photodegradation capacity and percent degradation was given by

$$q_e = \frac{(C_o - C_e)V}{W} \quad (2)$$

$$\%R = \frac{C_o - C_e}{C_o} \times 100 \quad (3)$$

where q_e is the photodegradation capacity of GG-Alg@Ag (mg g^{-1}); the initial and final concentration of MB after the operation is represented by C_o and C_e (mg L^{-1}); the volume of the sample taken is V and the catalyst dose be equal to W (g). $\%R$ is the photodegradation percentage after the assessment of supernatant through the UV-vis spectrophotometer at 662 nm.

2.5. Non-linear chi-square (χ^2) test and the sum of squares of error (SSE)

Nonlinear regressions, for example, the chi-square (χ^2) test, typically includes the minimization or boost of error appropriation between the test information and the anticipated isotherm dependent on its confluence criteria.[38] Nonlinear chi-square, χ^2 test, is a measurable mistake investigation instrument important for the best fit of the photodegradation information. Little χ^2 numbers demonstrate that information from the isotherm model was like the test information, while a bigger number speaks to the variety of the trial information. The

benefit of utilizing a chi-square test was looking at all isotherms on a similar abscissa and ordinate.

$$\chi^2 = \frac{\sum_{i=1}^{n} \left(q_{e,\mathrm{cal}} - q_{e,\mathrm{exp}}\right)_i^2}{q_{e,\mathrm{exp}}} \qquad SSE = \sum_{i=1}^{n} \left(q_{e,\mathrm{cal}} - q_{e,\mathrm{exp}}\right)_i^2 \tag{4}$$

3. Results and discussion

3.1. Characterization of GG-Alg@Ag

Fig. S2† shows the FTIR spectra of guar gum, alginate, and GG-Alg@Ag. The FTIR spectrum of alginate showed a broad peak at 3422 cm^{-1}, which is a result of O–H stretching. This broadband indicates association as a result of –COOH groups. Other important peaks were observed at 2927 cm^{-1} (aliphatic C–H stretching), 1620 cm^{-1} (C–O stretching), 1406 cm^{-1} (RCO–O– stretching), and 1043 cm^{-1} (C–O–C stretching).[39] Similarly, the FT-IR spectra of guar gum display the peak at 3408 cm^{-1} due to –OH stretching, the peak at 2917 cm^{-1} due to aliphatic $-CH_2$ stretching and peaks at 1058 cm^{-1} due to C–O–C stretching vibrations.[40] The FTIR spectra of GG-Alg@Ag represents most of the peaks from alginate and guar gum with variable values in wavenumber and intensity due to blending (GG-Alg) and involvement of the blend in reducing and stabilizing Ag nanoparticles. The peaks at 590 cm^{-1} (Ag←$\ddot{O}$ coordination bond) and 1149 cm^{-1} due to RCO–OH stretching (blend of GG-Alg).[41] Moreover, the higher value of the C=O bond at 1639 cm^{-1} concerning 1620, 1625 cm^{-1}, also supports the involvement of a lone pair of oxygen in complex formation. The FTIR studies suggest that the establishment of the GG-Alg@Ag complex takes place *via* the formation of Ag←$\ddot{O}$ coordination bonds with plenty of –OH and $-COO^-$ groups.

Typical XRD spectra of GG-Alg@Ag have been given in Fig. S3,† which suggests a crystalline structure of the material. The 2 theta values at 26.74°, 31.13°, 37.11°, 43.29°, 63.49° and 76.52° with plane values (110), (111), (200), (200), (113) and (213) corresponds to the characteristic peaks. The XRD structure and miller index values suggest that the Ag forms a distorted face-centered cubic structure (FCC) with GG-ALG blend through coordination bonds of the type Ag←$\ddot{O}$.[42]

A widely used mathematical function known as the Scherrer equation was utilized for the quantification of the nanocrystalline size of GG-ALG@Ag which is given as follows;[43]

$$t = \frac{k\lambda}{d\ \cos\ \theta} \tag{5}$$

where t= particle size (nm), k= geometric factor 0.9 for spherical shape, λ= the X-ray wavelength used Cu/K α = 0.154 nm,

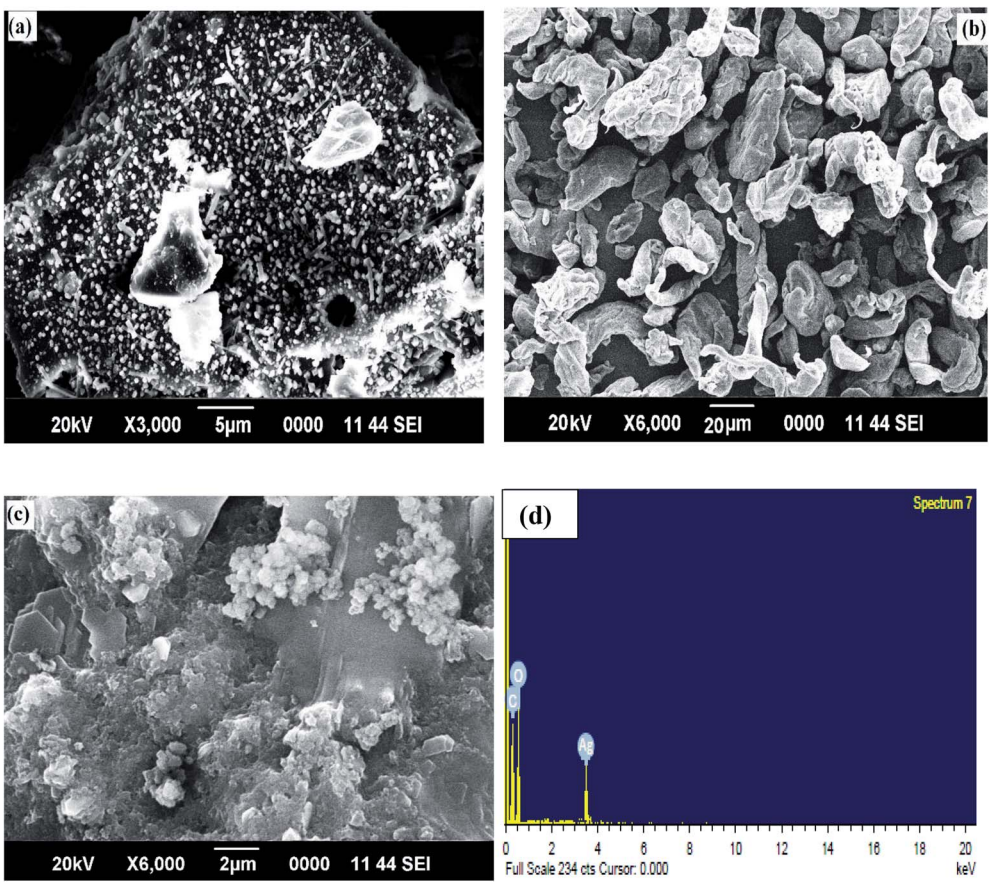

Fig. 1 SEM images of (a) alginate (b) guar gum (c) GG-Alg@Ag (d) EDX spectrum containing binding energies of Ag, C and O.

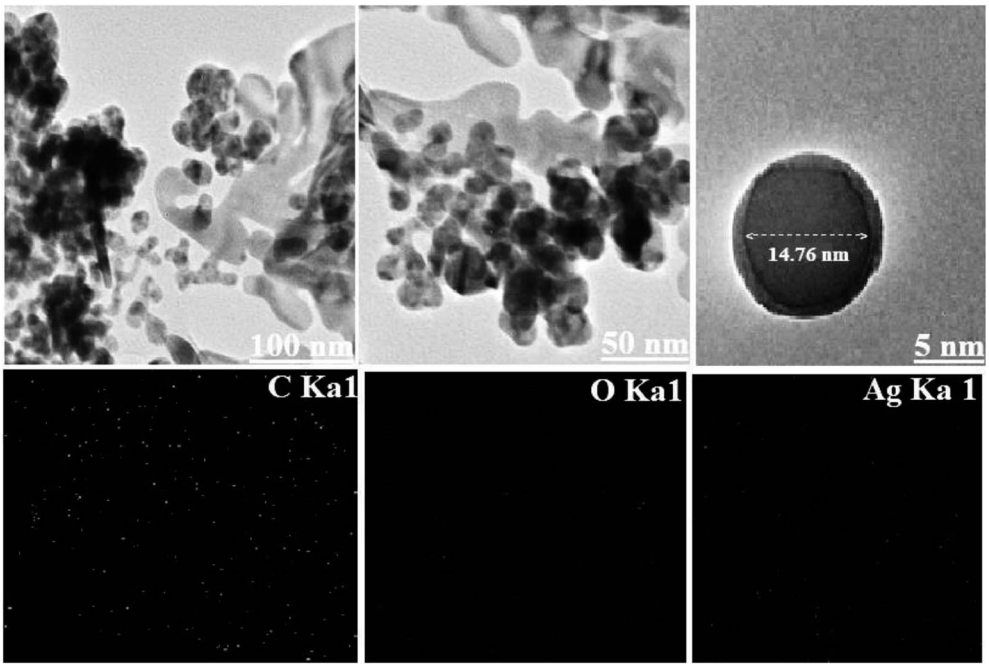

Fig. 2 The HRTEM images of GG-Alg@Ag bionanocomposite at different magnification range with corresponding elemental mapping of carbon, oxygen and Ag.

d = full width half maximum value, $\theta = 2\theta/2$. Using the peak corresponding to (hkl) value of (200), the size of the Ag nanoparticles supported GG-Alg blend was found to be 13.87 nm, which is in close agreement with the results obtained by TEM analysis.

Surface morphological studies of the alginate, guar gum, and GG-Alg@Ag with elemental analysis are shown in Fig. 1(a–c). The SEM image in Fig. 1(a) shows that the alginate has a regular spherical and cubical surface with uniform distribution. The surface morphology of neat guar gum was assessed under SEM, and distinctive granules with irregular geometry and size were observed in Fig. 1(b). Most of the granules were of elliptical size with non-porosity and a high degree of solidification. The highly porous and spherical shaped surface of GG-Alg@Ag in Fig. 1(c) suggests that the Ag NPs have a layer of GG-Alg blend that not only stabilizes them but also provides surface functional density. The elemental analysis of material has been performed using EDX spectroscopy given in Fig. 1(d). Strong signals were obtained from silver atoms at around 3.5 keV which correspond to the binding energy of Ag $L_{\beta 2}$ *i.e.* silver metallic nanocrystals. The results obtained are in close agreement with EDX spectra of Ag NPs and origination of other signals by C and O are due to presence of GG-Alg biopoplymer blend substituted with the Ag NPs.[44]

Zeta's potential estimation of GG-Alg@Ag in the KCl solution demonstrates that the point of zero charges of the material occurs at approximately pH = 4.45 (Fig. S4†). From the electroactive consequences shown in Fig. S4,† it is seen that MB is artificially adsorbed onto GG-Alg@Ag at pH values greater than 4.45. For a pH between 4 and 6, the adsorption is by all accounts a result of electrostatically coupled chemical communications. Therefore, the speciation of MB, just as the hydrolysis process on the GG-Alg@Ag surface, is essential to consider to explain the machinery of the photodegradation process.

The probable size of the particle and its distribution concerning a polymer matrix can be elucidated by using transmission electron microscopy (TEM) shown in Fig. 2. The tiny spherical point groups of 14.76 nm (also proved by XRD) were localized by TEM, which appears to be finely distributed in the GG-Alg biopolymer matrix. The image also represents some amount of aggregations in some regions, which may be due to the presence of a GG-Alg biopolymer blend responsible for the reduction and stabilization of AgNPs. Further the material was characterized by elemental mapping analysis. The mapping results revealed that in the electron micrograph region of synthesized material Fig. 1(c) the atomic distribution of Ag NPs are 28.56%.

The TGA-DTG thermogram of the material within a temperature range of 25–600 °C is shown in Fig. S5.† It is seen that the debasement of the material occurs in two stages. It is seen from the TGA bend that a noticeable weight reduction of the material occurs at 250–430 °C. There is no weight reduction below 250 °C or above 430 °C. It tends to be, for the most part, ascribed to the disappearance of water and natural segments related to the GG-Alg blend. Overall, the TGA results demonstrate a loss of 90% up to 407.93 °C. The DTG plot shows a serious sharp top at 250–430 °C, which is predominantly credited to the crystallization of silver nanoparticles topped with GG-Alg globules. DTG profiles demonstrate the occurrence of total warm disintegration and crystallization of the material.

For Ag nanoparticles, it has been observed earlier[45–47] that from TGA curve, the dominant weight loss of the Ag occurred in temperature region between 200 and 300 °C. There is almost no weight loss below 200 °C and above 300 °C. Therefore, in our

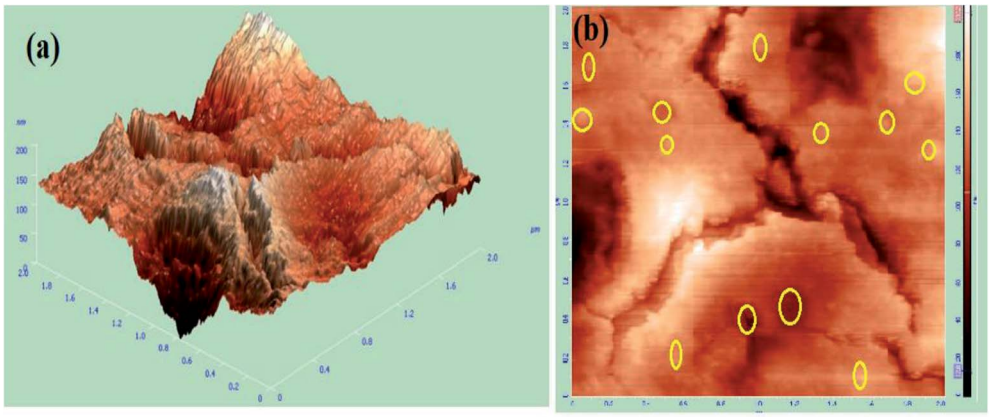

Fig. 3 (a) 3D topographical atomic force microscopic (AFM) image, (b) 2D AFM topographical image of GG-Alg@Ag bionanocomposite.

bionanocomposite, the decomposition of Ag might be in the similar range, and the majority of weight loss is due to the biopolymer which resulted from minute amount of Ag nanoparticles used in the bionanocomposites. However, it was observed that the bionanocomposites containing Ag is more thermally stable than that of pure polymer, so, Ag improved the thermal properties of the bionanocomposites.

Atomic force microscopy (AFM) is a complementary advancement to the information gathered by SEM analysis. In this study, AFM was utilized to assess the surface morphology and surface roughness of Ag NPs supported by the GG-Alg blend. Fig. 3(a and b) represents the 3D (1 μm × 1 μm) and 2D topographical images of GG-Alg@Ag bionanocomposite. With an average roughness value of 20.35 nm, Fig. 3(a) forms a close correlation with SEM results suggesting that the AgNps are adequately stabilized and functionalized by the GG-Alg blend. The yellow circled patches in Fig. 3(b) suggested an excellent spherical distribution of AgNPs in the GG-Alg biopolymer matrix with a root mean square value of 27.43 nm.[48]

3.2. Statistical analysis of model

RSM is an extensive collection of scientific and factual methods for the development and streamlining of parameters for different substances and modern processes.[49] The central composite design is a standout amongst the most dominant and productive trial structures among the other response surface plans because of its capacity to evaluate the quadratic model parameters, workings of consecutive structures, model detection for lack of fit, and utilization of squares. A design consisting of 30 experimental patterns based on a variation in four crucial variables such as time (*A*), pH (*B*), MB concentration (*C*), and catalyst dose (*D*) was constructed using Design Expert as listed in Table S2.† The given ranges for variable parameters such as exposure time (20–180 min), pH (1–9), MB concentration (50–250 mg L^{-1}), and catalyst dose (0.045–0.145 g) are listed in Table S2.† Based on the experimental and predicted results, a quadratic equation was obtained by operating a response function of four variables concerning their interactions during the process.

Table 1 Analysis of Variance (ANNOVA) for regression model

Source	Sum of squares	df	Mean square	*F* value	*p*-value prob > *F*	Significance
Model	1264.52	14	90.32	22.55	<0.0001	Significant
A-Time	151.35	1	151.35	37.79	<0.0001	
B-pH	7.23	1	7.23	1.80	0.1991	
C-conc.	48.71	1	48.71	12.16	0.0033	
D-dose	211.17	1	211.17	52.73	<0.0001	
AB	0.31	1	0.31	0.076	0.7862	
AC	0.78	1	0.78	0.19	0.6655	
AD	3.91	1	3.91	0.98	0.3387	
BC	12.41	1	12.41	3.10	0.0987	
BD	11.17	1	11.17	2.79	0.1156	
CD	39.47	1	39.47	9.86	0.0068	
A^2	104.55	1	104.55	26.11	0.0001	
B^2	688.43	1	688.43	171.90	<0.0001	
C^2	124.28	1	124.28	31.03	<0.0001	
D^2	43.19	1	43.19	10.79	0.0050	
Residual	60.07	15	4.00			
Lack of fit	60.05	10	6.01	1491.33	0.703	Not significant
Pure error	0.020	5	4.027×10^{-3}			
Cor total	1324.59	29				

Table 2 Statistical parameters for model

Std. dev.	2.00	*R*-squared	0.96
Mean	19.97	Adj *R*-squared	0.92
C. V.%	10.02	Pred *R*-squared	0.84
PRESS	345.92	Adeq precision	15.58
−2 log likelihood	105.97	BIC	156.98
		AICc	170.25

$$R1 = 28.24 + 2.51A - 0.55B + 1.42C - 2.97D - 0.14AB + 0.22AC - 0.49AD + 0.88BC + 0.84BD - 1.57CD - 1.95A^2 - 5.01B^2 - 2.13C^2 - 1.25D^2 \quad (6)$$

In eqn (6), a negative sign suggests an opposing impact, though a positive sign demonstrates a synergistic effect[39]. As in eqn (6), the time (A) and concentration (C) are pragmatic. This shows that the adsorption of MB by GG-Alg@Ag can be improved when these components are expanded. A higher value of T by a lower P value given in Table S3† was used to assess the importance of each coefficient.[50] A genuinely high mutuality between the test and anticipated response recommends the sufficiency of the fitted quadratic model.[51]

3.3. Analysis of variance

The interaction effect and the statistical significance of each term in the obtained quadratic model on MB photodegradation are expressed in the analysis of variance (ANOVA) of Table 1. The relevance of the regression model and corresponding coefficient terms was estimated by F and P values using Fisher's null hypothesis method.[52] A higher relevance of the regression model and each coefficient was dictated by a higher F value and lower P-value.[50] It was perceived that the model recommended by the RSM coupled with CCD is highly relevant, as indicated by the larger F value of 22.55 and a lower P-value of 0.00. An adequate precision value of 15.58 in the quadratic regression model imputed an adequate signal of photodegradation of MB on the GG-Alg@Ag. The distinction of the lack of fit is not a relevant result having a $p > 0.05$, which is statistically irrelevant. The sufficiency of the model was evaluated by the estimations of the relationship coefficient R^2 and R_{adj}^2. In light of the results perceived using ANOVA, the estimations of R^2 and R_{adj}^2 were observed to be 0.96 and 0.92, as given in Table 2. The high estimation of R^2 advocates a connection amongst the trial and anticipated estimations of reaction. The estimation of R_{adj}^2 demonstrates that 92.33% of the MB evacuation is because of individual factors aside from the 7.67% of the variation that could not be clarified by the model.

$$R1 = 28.24 + 1.42C - 2.97D - 1.95A^2 - 2.13C^2 - 1.25D^2 \quad (7)$$

A plot between actual values accessed by the designed experiments and predicted estimations computed by the model is shown in Fig. 4(a). Fig. 4(b) constitutes the normal probability *vs.* studentized residual plot for assessing the approximation of the real system by the models can be found in Fig. 4(b); points circulating along the straight line without a response exchange appear as a typical appropriation curve of residuals. The diagram demonstrates good conveyance of the points along the straight line with the estimations of R^2 and R_{adj}^2 as 0.96 and 0.92, respectively.

3.4. Three-dimensional response surface plot and their interpretation

Three-dimensional (3D) surface plots are the graphical portrayal of regression equations delineating the synchronous impact of two variables on adsorption while keeping the other variables constant.[52] 3D surface plots of the interdependence effect of variables on the degradation capacity of MB are shown in Fig. 5(a–d). Fig. 5(a) shows a 3D surface plot of the simultaneous effect of pH and time on the degradation capacity of MB while holding the catalyst dose to 0.07 g, the MB concentration

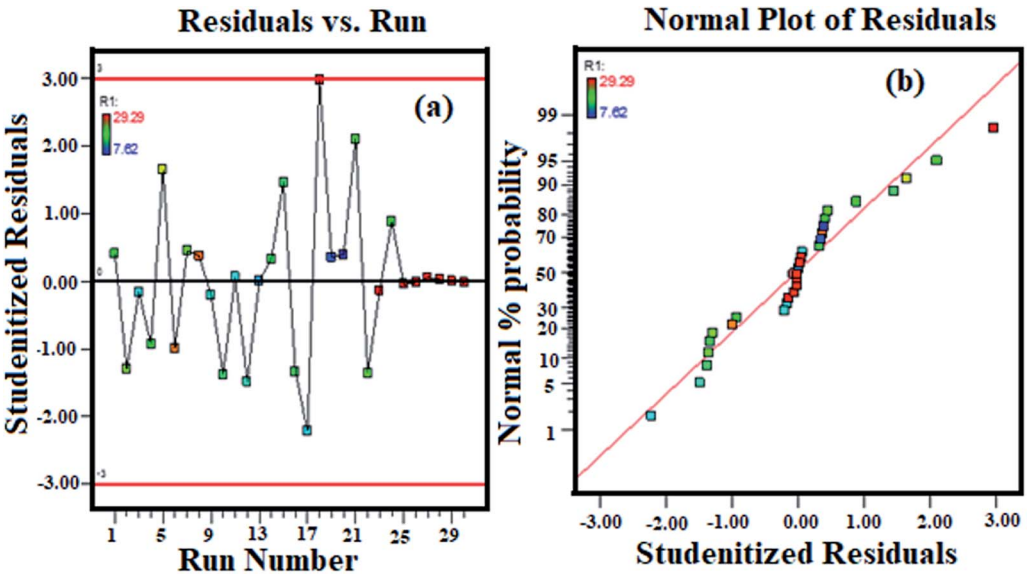

Fig. 4 (a) Correlation between actual and predicted values and (b) normal probability plot of studentized residuals.

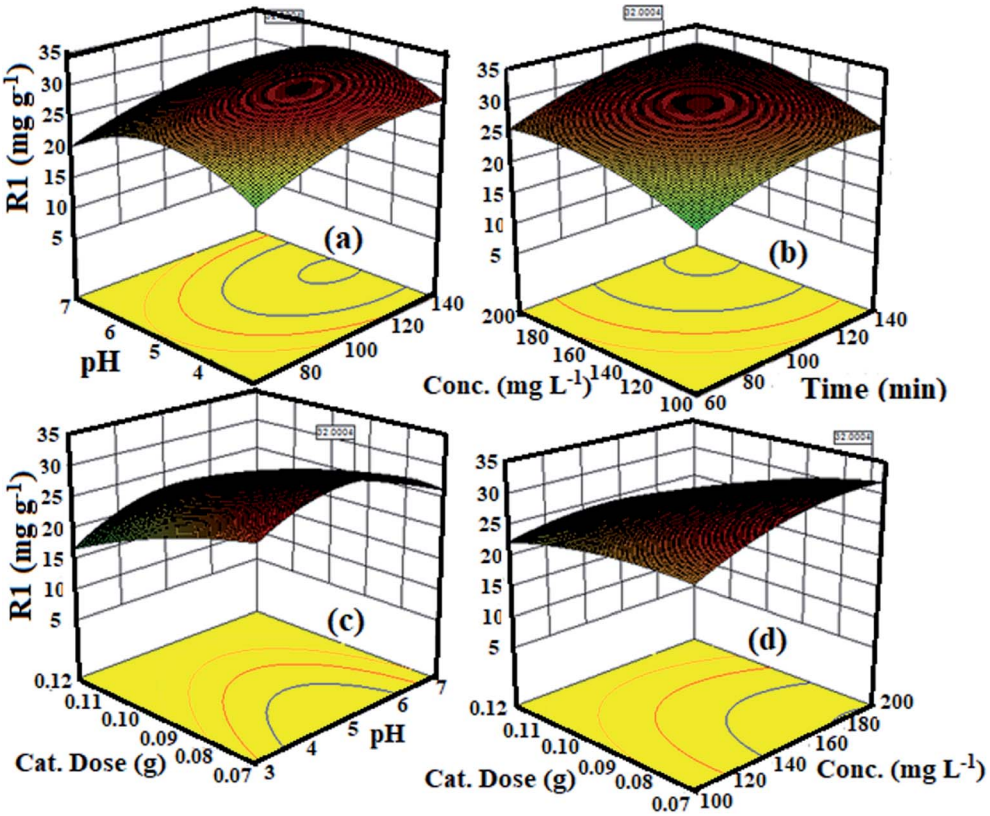

Fig. 5 3D surface plot for the interactive effect of (a) pH and time (b) concentration and time (c) dose and pH and (d) dose and conc. on the degradation capacity of MB by GG-Alg@Ag bionanocomposite.

to 194 mg L^{-1}, and the temperature at 55 °C. From Fig. 5(a), it can be seen that the degradation limit of MB increases as pH values increase from 2 to 6 and after which, it declines somewhat with the further increase in pH. At pH < 3.0, H^+ ions emulate with MB cationic dye for the available active sites on the external interface of the catalyst, which impedes the reach of MB because of the repulsion forces.[42] Hence, the evacuation of MB was less presumably because of the increased rivalry of protons with MB dye for surface active sites. As the pH of the system further increases, the concentration of H^+ particles in the dissolvable medium abates, which accelerates the adsorption of MB. The higher adsorption rate at a high pH suggests that MB connects with adsorbent through a chelating component with carboxylic and hydroxyl functions of the catalyst until the greatest yield is reached. At pH > 5.0, an abatement in the adsorption rate was observed, which might be ascribed to support of the MB with hydroxides.[53] Similarly, from Fig. 5(b), an expansion in percent effectiveness of MB degradation was observed when the concentration of MB increased from 100 to 200 mg L^{-1} with an increase in time from 60 to 140 min. A further increase in MB concentration leads to a decrease in percent degradation because of the saturation of the external surface sites of the catalyst by dye molecules at a limited concentration.[54] Thus, an optimized MB concentration of 194 mg L^{-1} was used for all the adsorption isotherm, kinetic, and thermodynamic studies. Fig. 5(c) shows the 3D surface plot of the cooperative impact of pH and catalyst portion on the evacuation proficiency of MB while holding the time to 120.24 min, the MB concentration to 194 mg L^{-1}, and the temperature at 55 °C. It can be observed that an increasing catalyst dose from 0.07 g to 0.12 g with an increase in pH decreases the degradation capacity for MB. This conduct can be clarified as to when the catalyst amount increases, the number of catalyst particles likewise increases, encouraging increasingly dynamic sites for adsorption. Given this, as the amount of adsorbent increases, the effectual surface area and adsorbate/adsorbent proportion decrease resulting in less MB take-up. Fig. 5(d) shows the 3D interdependent plot between the catalyst dose and MB concentration regarding the expulsion proficiency of MB. It can be observed that as the concentration increases from 100 to 200 mg L^{-1} the dye removal efficiency increases while the increase in catalyst dose restricts the degradation capacity, suggesting that MB concentration has a synergistic effect while the adsorbent dose has an antagonistic effect. The purpose of this experiment was to optimize the four variables that affect the photodegradation of MB on GG-Alg@Ag. Results obtained clearly suggest that optimized values of an irradiation time of 120 min, a pH of 4.98, a catalyst dose of 0.07 g, and a concentration of MB of 194 mg L^{-1}. With respect to these circumstances, the predicted removal percentage of MB dye by GG-Alg@Ag was 32.00 mg g^{-1} which

agrees well with the experimental value of 29.29 mg g^{-1} with a desirability of 1.0.

3.5. Adsorption kinetics

Kinetic experiments were performed to determine the degradation rate of MB onto the GG-Alg@Ag bionanocomposite. Kinetic studies were administered utilizing the pseudo-first-order and pseudo-second-order models.[55,56] The mathematical functions for both the models are given by eqn (8) and (9) as follows:

$$q_t = q_e(1 - e^{-k_1 t}) \quad (8)$$

$$q_t = \frac{k_2 q_e^2 t}{1 + k_2 q_e t} \quad (9)$$

where k_1 (min^{-1}) and k_2 (g mg^{-1} min^{-1}) are the pseudo-first-order and pseudo-second-order rate constants, while q_e and q_t (mg g^{-1}) are the degradation limit at equilibrium and that after time t (min), respectively. The estimations of kinetic parameters and curves are abridged in Table S4† and Fig. 6(b). It is obvious from Table S4† that for the pseudo-second-order, there is a high estimation of $R2$ (0.99) and low estimation of χ^2 (0.99) and SSE (0.48) in contrast with the pseudo-first-order active model for MB, showing that the adsorption of MB pursued the pseudo-second-order. Also, hypothetical estimations of q_e are near the test q_e values for pseudo-second request energy showing that the pseudo-second request model fits well with the trial photodegradation information for MB and the adsorption occurs *via* the development of solid-substance bond. Fig. 6(a) represents the action curve for the photodegradation of MB by GG-Alg@Ag BNC with respect to time for a MB concentration of 40, 80, 120, 160 and 194 mg L^{-1}. It was observed that by stepping from 40–194 mg L^{-1} MB concentration the maximum photodegradation capacity (%) continuously raised as 88.70% for 40, 89.83% for 80, 90.58% for 120, 91.53% for 160 and 93.24% for 194 mg L^{-1} with time variation of 5–120 min under

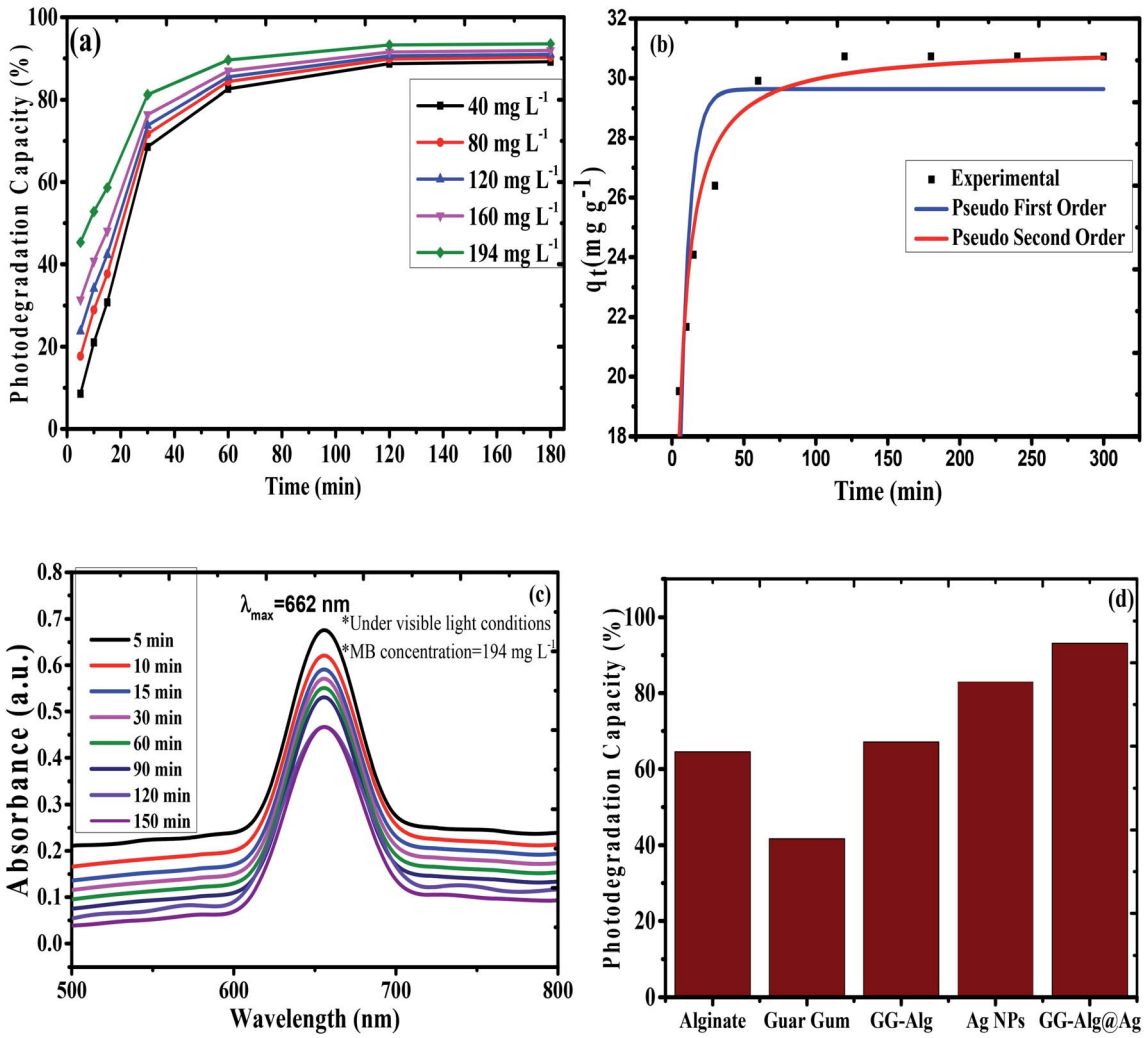

Fig. 6 (a) Plot of photodegradation capacity of GG-Alg@Ag with respect to time for different concentration of MB under visible light conditions (b) non-linear regression plot of pseudo first order and pseudo second order for MB onto GG-Alg@Ag pH (4.98), MB concentration (194 mg L^{-1}) and catalyst dose (0.07 g) (c) UV-vis action curve for MB degradation by GG-Alg@Ag BNC at 194 mg L^{-1} MB concentration with respect to time and (d) graph showing photodegradation capacity of GG-Alg@Ag bionanocomposite and its individual component.

Table 3 Comparison of photodegradation capacity with other materials in literature

Adsorbent	Kinetic model	Photodegradation capacity (%)	References
Anionic silver nanoparticles	Pseudo first order	75%	57
Ag/ZnO nanoparticles	Pseudo first order	82.6	58
Ag/AgCl@ZIF-8	Pseudo first order	90%	59
Ag/SnO_2 nanoparticles	Pseudo first order	84%	60
Silver molybdates	Diffusion	90%	61
ZnO microstructures with Ag	Pseudo first order	87.7%	62
GG-Alg@Ag	Pseudo second order	92.33%	Present work

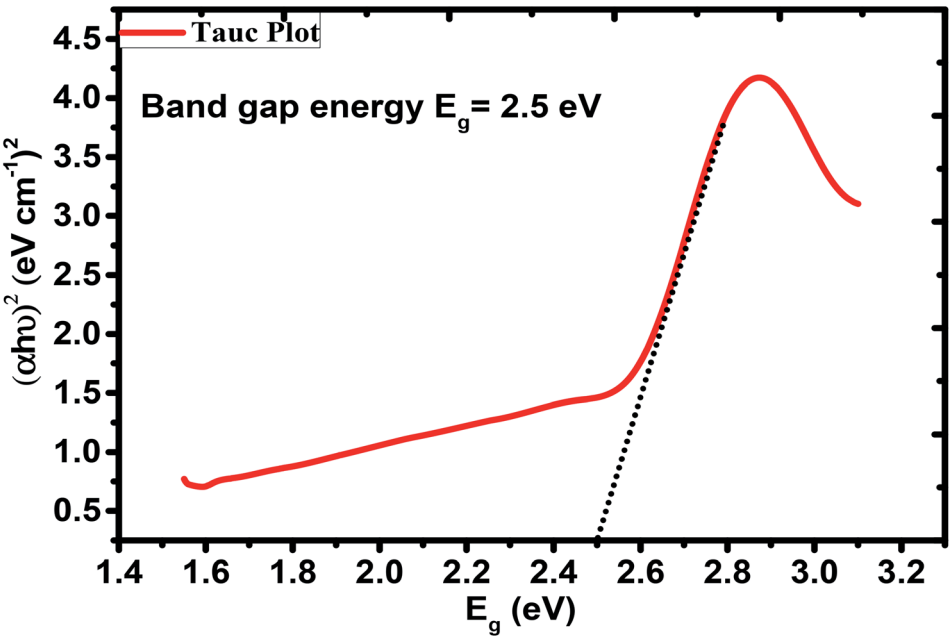

Fig. 7 Tauc's Plot for bandgap energy of GG-Alg@Ag bionanocomposite.

visible light conditions. The maximum capacity of 93.24% also shows a close agreement of the capacity 92.33% obtained by using CCD-RSM module. From Fig. 6(c) it is observed that with respect to passage of time under the visible light the absorbance value is continuously decreasing which belongs to the photodegradation of MB. Fig. 6(d) represents the photodegradation capacity of GG-Alg@Ag bionanocomposite and its individual component under visible light conditions. From the graph that the photodegradation capacity for alginate 64.52% (due to presence of –COOH groups), guar gum 41.37% (due to –OH groups), GG-Alg blend 67.13% (combined synergetic effect of both –OH and –COOH groups), Ag NPs 82.97% (metallic silver due to vacancy creation under visible light) and GG-Alg@Ag 93.05% (combined synergetic effect GG-Alg blend towards silver) was observed which suggest that the blending of alginate and guar gum with Ag NPs provide better facilitation to degrade the methylene blue dye photocatalytically.

3.6. Comparison with other materials

Table 3 compares the optimal capacity of the synthesized GG-Alg@Ag bionanocomposite to those of the previously reported materials. As can be observed from Table 3, GG-Alg@Ag shows significant improvements over the existing materials for the removal of MB dye. The high photodegradation efficiency of the readied GG-Alg@Ag bionanocomposite together with their proper qualities, for example, reusability, simple combination, simple detachment, and eco-friendly composition, make them appropriate options in contrast to the outstanding and generally utilized catalysts for the expulsion of MB from water systems.

3.7. Optical analysis and mechanism of photodegradation

Using UV-vis absorption spectrophotometry, the bandgap energy (E_g) of the GG-Alg@Ag bionanocomposite were determined by using Tauc's equation given as follows[59]

$$(\alpha h\nu) = A(h\nu - E_g)^n \quad (10)$$

where α is the absorption coefficient, h is the Planck constant, ν is the frequency of radiation, A is the constant, n is a constant of transitions variance, *e.g.* for directly allowed transition $n = 1/2$, for indirectly allowed transition $n = 2$. In this study, we have taken $n = 1/2$, and when plotted a graph between $(\alpha h\nu)^2$ and $h\nu$,

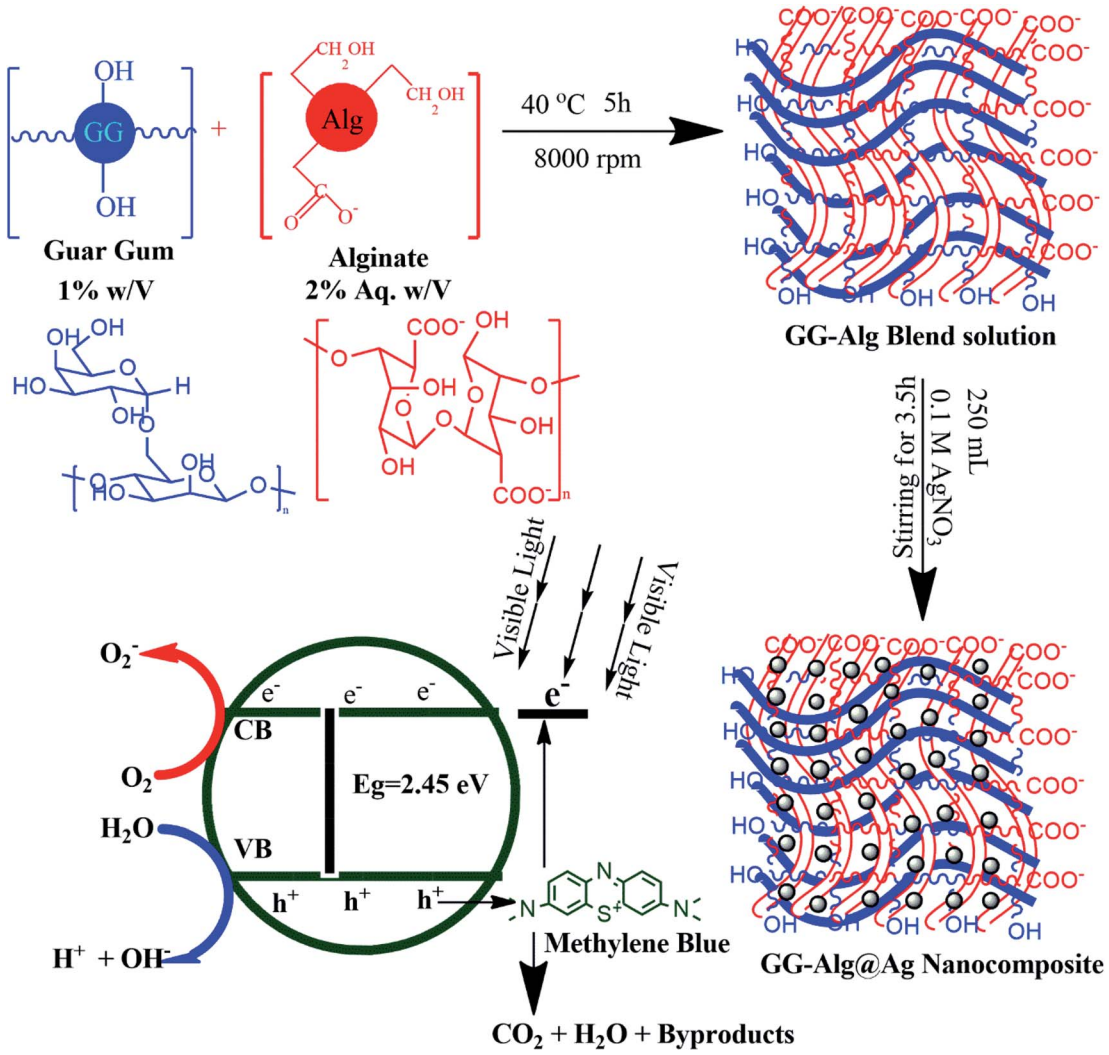

Fig. 8 Proposed mechanism for synthesis and photocatalytic activity of GG-Alg@Ag bionanocomposite.

the intercept value gives the bandgap energy of the material. Fig. 7 represents the Tauc plot indicating a value of $E_g = 2.5$ eV for the GG-Alg@Ag bionanocomposite. Generally, for bare Ag NPs, the E_g was found to be 3.45 eV, so the lowering in bandgap value can be due to decrement in quantum confinement by functionalization of Ag NPs with GG-Alg blend.[63,64]

When GG-Alg@Ag absorb visible light of the solar spectra, the surface electrons from the outer sp band are excited to the next energy level because of SPR results;[65,66] these electrons are promptly accepted by the oxygen (O_2) molecules to create oxygen radicals (O_2) that attack and degrade the MB dye molecules as projected by reaction (i)–(x). Besides, the holes generated within the 5sp orbital are filled by electrons accepted[56] from the absorbable photosensitized dye particle, thus debasing the MB. Retention of visible light from the sun by the Ag NPs causes the excitation of electrons from the 4d orbital to the 5sp orbital. This inter-band progress results in the excitation of the numerous photogenerated electrons. These excited electrons act with the oxygen molecules to create oxygen radicals (O_2) and, therefore, the OH^- ions to create hydroxyl (OH) radicals. Thus, fashioned radicals attack the dye molecule coupled onto the exterior interface of the Ag NPs, resulting in degradation of the dye. Additionally, during the deterioration of the dye by the free radicals, the holes generated within the d orbital of the Ag NPs are filled by electrons accepted from the adsorbable dye molecule, resulting in more degradation of the MB dye.[65] Thus, the Ag NPs are primed for the absorption of the total light spectrum because of the SPR result, and therefore the inter-band transition of 4d electrons to the 5sp band.[66] This photocatalytic mechanism by visual sunlight irradiation *via* Ag NPs within the degradation of MG dye is conferred in (i)–(x).

$$Ag + h\nu \xrightarrow{\text{sunlight}} Ag(e_{CB}^- + h_{VB}^+) \quad \text{(i)}$$

$$Ag(h_{VB}+) + H_2O \rightarrow Ag + H^+ + OH^{\cdot} \quad \text{(ii)}$$

$$Ag(h_{VB}+) + OH^- \rightarrow Ag + OH^{\cdot} \quad \text{(iii)}$$

$$Ag(e_{CB}-) + O_2 \rightarrow Ag + O_2^{\cdot -} \quad \text{(iv)}$$

$$O_2^{\bullet -} + H^+ \rightarrow HO_2 \quad \text{(v)}$$

$$MB + Ag \xrightarrow{\text{sunlight}} MB^{\bullet +} e_{CB}^{-}(Ag) \quad \text{(vi)}$$

$$O_2 + e^- \rightarrow O_2^{\bullet -} \quad \text{(vii)}$$

$$MB^{\bullet +} + OH^- \rightarrow MB + OH^{\bullet} \quad \text{(viii)}$$

$$MB^{\bullet +} + OH^{\bullet} \rightarrow \text{products} \quad \text{(ix)}$$

$$MB^{\bullet +} + O_2^{\bullet -} \rightarrow \text{products} \quad \text{(x)}$$

The coupling of the dye molecules over the exterior interface of GG-Alg@Ag bionanocomposite directly affects the occurrence of the exchange of electrons between the excited dye and Ag, which further accelerates the degradation rate.[67] The $OH^{\bullet}$ radicals will attack the C–S^+=C reactive group in MB, which is in direct electrostatic association with the exterior interface of the GG-Alg@Ag bionanocomposite. Thus, the underlying stage of MB debasement is attributed to the cleavage of the bonds of the C–S^+=C reactive group in MB. The transformation from C–S^+=C to C–S(=O)– C needs the protection of the covalent bond conjugation, which prompts the opening of the central aromatic ring associated with the heteroatoms S and N. The origin of H atoms necessary for C–H and N–H bond formation is projected from the proton reduction by photogeneration as proposed by Fig. 8.[68]

4. Conclusions

This experimental study researched the photodegradation of MB on GG-Alg@Ag bionanocomposite. Investigations were completed assessing various adsorption parameters (pH, focus, catalyst mass, and radiation time with sunlight). RSM coupled with a central composite model was utilized to analyze the concurrent effect of four factors on MB evacuation. It was demonstrated that a second-order polynomial regression model could appropriately decipher the test information with a coefficient of assurance ($R2$) estimation of 0.96 and an F-estimation of 22.55. The concurrent advancement of the multi-reaction framework by an attractive quality capacity showed that 92.33% evacuation of MB is conceivable utilizing the ideal states of a pH = 4.98, an MB concentration of 194 mg L^{-1}, a radiation time of 120 min, and a catalyst amount of 0.07 g. The Langmuir and Freundlich adsorption isotherm models were utilized for the depiction of the adsorption equipoise of MB. The information highly concurred with the Langmuir isotherm. The adsorption information was constrained by both pseudo-first-order and pseudo-second-order models. The kinetic exams demonstrated that the rate of the reaction for the evacuation of MB pursued the second-order model well. This investigation demonstrates that the CCD model is appropriate to improve the experiments of MB evacuation by photodegradation. The optical studies indicated a value of 2.5 eV by Tauc's plot for bandgap energy (E_g) for GG-Alg@Ag bionanocomposite. These results suggest that composites have promising applications in the expulsion of MB from wastewater because of the effective and rapid photocatalytic movement, similar to simple recovery, and can be explored in industrial applications on a large scale.

Conflicts of interest

There are no conflicts to declare.

Acknowledgements

The authors appreciatively recognize Chandigarh University Gharuan Mohali, instrumentation lab, a place for excellence in nanomaterials division of applied physics AMU, Sophisticated Analytical instrumentation office (SAIF) Punjab University Chandigarh, STIC, Cochin University. The authors extend their appreciation to the Deanship of Scientific Research at King Saud University for funding this work through research group No RG-1438-006.

References

1 H. M. Zidan, N. A. El-Ghamaz, A. M. Abdelghany and A. L. Waly, Photodegradation of Methylene Blue with PVA/PVP Blend under UV Light Irradiation, *Spectrochim. Acta, Part A*, 2018, **199**, 220–227.
2 M. S. Ali, H. A. Al-Lohedan, M. M. S. Abdullah, Z. Afsan and S. Tabassum, Catalytic Induced Morpholical Transformation of Porous ZnO to ZnO Nanorods by Sn(IV) and Their Effect on Photocatalytic Reduction of Methylene Blue and DFT Calculations, *Spectrochim. Acta, Part A*, 2019, **220**, 117101.
3 N. Nasuha, S. Ismail and B. H. Hameed, Activated Electric Arc Furnace Slag as an Effective and Reusable Fenton-like Catalyst for the Photodegradation of Methylene Blue and Acid Blue 29, *J. Environ. Manage.*, 2017, **196**, 323–329.
4 B. Pava-Gómez, X. Vargas-Ramírez and C. Díaz-Uribe, Physicochemical Study of Adsorption and Photodegradation Processes of Methylene Blue on Copper-Doped TiO_2 Films, *J. Photochem. Photobiol., A*, 2018, **360**, 13–25.
5 D. Majumder, I. Chakraborty, K. Mandal and S. Roy, Facet-Dependent Photodegradation of Methylene Blue Using Pristine CeO_2 Nanostructures, *ACS Omega*, 2019, **4**(2), 4243–4251.
6 Y. Geng, J. Zhang, J. Zhou and J. Lei, Study on Adsorption of Methylene Blue by a Novel Composite Material of TiO_2 and Alum Sludge, *RSC Adv.*, 2018, **8**(57), 32799–32807.
7 T. Larbi, K. Doll and M. Amlouk, Temperature Dependence of Raman Spectra and First Principles Study of $NiMn_2O_4$ Magnetic Spinel Oxide Thin Films. Application in Efficient Photocatalytic Removal of RhB and MB Dyes, *Spectrochim. Acta, Part A*, 2019, **216**, 117–124.
8 Z. Ma, L. Deng, G. Fan and Y. He, Hydrothermal Synthesis of P-C_3N_4/f-BiOBr Composites with Highly Efficient Degradation of Methylene Blue and Tetracycline, *Spectrochim. Acta, Part A*, 2019, **214**, 103–110.
9 Saruchi, V. Kumar, B. S. Kaith and R. Jindal, Synthesis of Hybrid Ion Exchanger for Rhodamine B Dye Removal:

Equilibrium, Kinetic and Thermodynamic Studies, *Ind. Eng. Chem. Res.*, 2016, **55**(39), 10492–10499.

10 X. Li, X. Jin, N. Zhao, I. Angelidaki and Y. Zhang, Novel Bio-Electro-Fenton Technology for Azo Dye Wastewater Treatment Using Microbial Reverse-Electrodialysis Electrolysis Cell, *Bioresour. Technol.*, 2017, **228**, 322–329.

11 C. Anushree and J. Philip, Efficient Removal of Methylene Blue Dye Using Cellulose Capped Fe_3O_4 Nanofluids Prepared Using Oxidation-Precipitation Method, *Colloids Surf., A*, 2019, **567**, 193–204.

12 S. Xu, H. Lu, L. Chen and X. Wang, Molecularly Imprinted TiO_2 hybridized Magnetic Fe_3O_4nanoparticles for Selective Photocatalytic Degradation and Removal of Estrone, *RSC Adv.*, 2014, **4**(85), 45266–45274.

13 G. Fan, J. Luo, L. Guo, R. Lin, X. Zheng and S. A. Snyder, Doping Ag/AgCl in Zeolitic Imidazolate Framework-8 (ZIF-8) to Enhance the Performance of Photodegradation of Methylene Blue, *Chemosphere*, 2018, **209**, 44–52.

14 G. Sharma, A. Kumar, S. Sharma, M. Naushad, T. Ahamad, S. I. Al-Saeedi, G. M. Al-Senani, N. S. Al-kadhi and F. J. Stadler, Facile Fabrication of $Zr_2Ni_1Cu_7$ Trimetallic Nano-Alloy and Its Composite with Si_3N_4 for Visible Light Assisted Photodegradation of Methylene Blue, *J. Mol. Liq.*, 2018, **272**, 170–179.

15 N. Fathi, H. Almasi and M. K. Pirouzifard, Sesame Protein Isolate Based Bionanocomposite Films Incorporated with TiO_2 Nanoparticles: Study on Morphological, Physical and Photocatalytic Properties, *Polym. Test.*, 2019, **77**, 105919.

16 I. Hasan, F. A. Qais, F. M. Husain, R. A. Khan, A. Alsalme, B. Alenazi, M. Usman, M. H. Jaafar and I. Ahmad, Eco-Friendly Green Synthesis of Dextrin Based Poly (Methyl Methacrylate) Grafted Silver Nanocomposites and Their Antibacterial and Antibiofilm Efficacy against Multi-Drug Resistance Pathogens, *J. Cleaner Prod.*, 2019, **230**, 1148–1155.

17 J. Saini, V. K. Garg and R. K. Gupta, Removal of Methylene Blue from Aqueous Solution by Fe_3O_4@Ag/SiO_2 Nanospheres: Synthesis, Characterization and Adsorption Performance, *J. Mol. Liq.*, 2018, **250**, 413–422.

18 Y. Yang, Q. Yan, Q. Liu, Y. Li, H. Liu, P. Wang, L. Chen, D. Zhang, Y. Li and Y. Dong, An Ultrasensitive Sandwich-Type Electrochemical Immunosensor Based on the Signal Amplification Strategy of Echinoidea-Shaped Au@Ag-Cu_2O Nanoparticles for Prostate Specific Antigen Detection, *Biosens. Bioelectron.*, 2018, **99**, 450–457.

19 T. Balkan, S. Kizir and D. Tuncel, One-Pot Synthesis of Hybrid Conjugated Oligomer-Ag Nanoparticles, *ACS Omega*, 2017, **2**(9), 5470–5477.

20 A. S. A. Al-Sherbini, H. E. A. Ghannam, G. M. A. El-Ghanam, A. A. El-Ella and A. M. Youssef, Utilization of Chitosan/Ag Bionanocomposites as Eco-Friendly Photocatalytic Reactor for Bactericidal Effect and Heavy Metals Removal, *Heliyon*, 2019, **5**(6), e01980.

21 P. Dong, X. Cheng, Z. Jin, Z. Huang, X. Nie, X. Wang and X. Zhang, The Green Synthesis of Ag-Loaded Photocatalyst *via* DBD Cold Plasma Assisted Deposition of Ag Nanoparticles on N-Doped TiO_2 Nanotubes, *J. Photochem. Photobiol., A*, 2019, **382**, 111971.

22 Z. Khan, Encapsulation of Silver Nanoparticles into the Helix of Water Soluble Starch and Their Sensing Properties, *Int. J. Biol. Macromol.*, 2019, **136**, 165–176.

23 J. Zhang, X.-X. Wang, B. Zhang, S. Ramakrishna, M. Yu, J.-W. Ma and Y.-Z. Long, In Situ Assembly of Well-Dispersed Ag Nanoparticles throughout Electrospun Alginate Nanofibers for Monitoring Human Breath—Smart Fabrics, *ACS Appl. Mater. Interfaces*, 2018, **10**(23), 19863–19870.

24 M. M. Solomon, H. Gerengi, T. Kaya and S. A. Umoren, Performance Evaluation of a Chitosan/Silver Nanoparticles Composite on St37 Steel Corrosion in a 15% HCl Solution, *ACS Sustainable Chem. Eng.*, 2017, **5**(1), 809–820.

25 M. Goswami, D. Baruah and A. M. Das, Green Synthesis of Silver Nanoparticles Supported on Cellulose and Their Catalytic Application in the Scavenging of Organic Dyes, *New J. Chem.*, 2018, **42**(13), 10868–10878.

26 P. Wang, Z. Geng, J. Gao, R. Xuan, P. Liu, Y. Wang, K. Huang, Y. Wan and Y. Xu, Zn_xCd_1-XS/Bacterial Cellulose Bionanocomposite Foams with Hierarchical Architecture and Enhanced Visible-Light Photocatalytic Hydrogen Production Activity, *J. Mater. Chem. A*, 2015, **3**(4), 1709–1716.

27 O. V. Mikhailov, Synthesis of Ag Nanoparticles under a Contact of Water Solution with Silver(I)Chloride Biopolymer Matrix, *J. Mol. Liq.*, 2019, **291**, 111354.

28 Y. Guesmi, H. Agougui, R. Lafi, M. Jabli and A. Hafiane, Synthesis of Hydroxyapatite-Sodium Alginate *via* a Co-Precipitation Technique for Efficient Adsorption of Methylene Blue Dye, *J. Mol. Liq.*, 2018, **249**, 912–920.

29 R. Ahmad and A. Mirza, Synthesis of Guar Gum/Bentonite a Novel Bionanocomposite: Isotherms, Kinetics and Thermodynamic Studies for the Removal of Pb(II) and Crystal Violet Dye, *J. Mol. Liq.*, 2018, **249**, 805–814.

30 N. Boukhalfa, M. Boutahala, N. Djebri and A. Idris, Maghemite/Alginate/Functionalized Multiwalled Carbon Nanotubes Beads for Methylene Blue Removal: Adsorption and Desorption Studies, *J. Mol. Liq.*, 2019, **275**, 431–440.

31 Z. Anfar, R. El Haouti, S. Lhanafi, M. Benafqir, Y. Azougarh and N. El Alem, Treated Digested Residue during Anaerobic Co-Digestion of Agri-Food Organic Waste: Methylene Blue Adsorption, Mechanism and CCD-RSM Design, *J. Environ. Chem. Eng.*, 2017, **5**(6), 5857–5867.

32 P. C. Bandara, E. T. Nadres and D. F. Rodrigues, Use of Response Surface Methodology To Develop and Optimize the Composition of a Chitosan–Polyethyleneimine–Graphene Oxide Nanocomposite Membrane Coating To More Effectively Remove Cr(vi) and Cu(II) from Water, *ACS Appl. Mater. Interfaces*, 2019, **11**(19), 17784–17795.

33 S. Sivalingam, T. Kella, M. Maharana and S. Sen, Efficient Sono-Sorptive Elimination of Methylene Blue by Fly Ash-Derived Nano-Zeolite X: Process Optimization, Isotherm and Kinetic Studies, *J. Cleaner Prod.*, 2019, **208**, 1241–1254.

34 D. Zhang, F. Wang, S. Cao and X. Duan, Investigation on Enhanced Photocatalytic Degradation of Bisphenol A with Bismuth Oxyiodide Catalyst Using Response Surface Methodology, *RSC Adv.*, 2018, **8**(11), 5967–5975.

35 A. Vanaamudan, M. Sadhu and P. Pamidimukkala, Chitosan-Guar Gum Blend Silver Nanoparticle Bionanocomposite with Potential for Catalytic Degradation of Dyes and Catalytic Reduction of Nitrophenol, *J. Mol. Liq.*, 2018, **271**, 202–208.

36 S. Chandran, V. Ravichandran, S. Chandran, J. Chemmanda and B. Chandarshekar, Biosynthesis of PVA Encapsulated Silver Nanoparticles, *J. Appl. Res. Technol.*, 2016, **14**(5), 319–324.

37 N. R. Singha, A. Dutta, M. Mahapatra, J. S. D. Roy, M. Mitra, M. Deb and P. K. Chattopadhyay, In Situ Attachment of Acrylamido Sulfonic Acid-Based Monomer in Terpolymer Hydrogel Optimized by Response Surface Methodology for Individual and/or Simultaneous Removal(s) of M(III) and Cationic Dyes, *ACS Omega*, 2019, **4**(1), 1763–1780.

38 A. Kaushal and S. K. Singh, Critical Analysis of Adsorption Data Statistically, *Appl. Water Sci.*, 2017, **7**(6), 3191–3196.

39 L. Wang, Y. Hou, X. Zhong, J. Hu, F. Shi and H. Mi, Preparation and Catalytic Performance of Alginate-Based Schiff Base, *Carbohydr. Polym.*, 2019, **208**, 42–49.

40 R. Ahmad and I. Hasan, L -Methionine Montmorillonite Encapsulated Guar Gum-g-Polyacrylonitrile Copolymer Hybrid Nanocomposite for Removal of Heavy Metals, *Groundwater for Sustainable Development*, 2017, **5**, 75–84.

41 J. Venkatesan, J.-Y. Lee, D. S. Kang, S. Anil, S.-K. Kim, M. S. Shim and D. G. Kim, Antimicrobial and Anticancer Activities of Porous Chitosan-Alginate Biosynthesized Silver Nanoparticles, *Int. J. Biol. Macromol.*, 2017, **98**, 515–525.

42 S. Muzaffar and H. Tahir, Enhanced Synthesis of Silver Nanoparticles by Combination of Plants Extract and Starch for the Removal of Cationic Dye from Simulated Waste Water Using Response Surface Methodology, *J. Mol. Liq.*, 2018, **252**, 368–382.

43 P. Scherrer, Estimation of the Size and Internal Structure of Colloidal Particles by Means of Rontgen Rays, *Nachrichten von der Gesellschaft der Wissenschaften zu Göttingen*, 1918, **26**, 98–100.

44 R. Geethalakshmi and D. V. L. Sarada, Gold and Silver Nanoparticles from Trianthema Decandra: Synthesis, Characterization, and Antimicrobial Properties, *Int. J. Nanomed.*, 2012, **7**, 5375–5384.

45 L. Gharibshahi, E. Saion, E. Gharibshahi, A. Shaari and K. Matori, Structural and Optical Properties of Ag Nanoparticles Synthesized by Thermal Treatment Method, *Materials*, 2017, **10**(4), 402.

46 V. V. Vodnik, J. V. Vuković and J. M. Nedeljković, Synthesis and Characterization of Silver - Poly(Methylmethacrylate) Nanocomposites, *Colloid Polym. Sci.*, 2009, **287**(7), 847–851.

47 B. Soni and S. Biswas, Stability of Microstructure at High Temperatures in Silver Nanoparticles Coated with an in Situ Grown Thin Graphitic Carbon Layer, *J. Alloys Compd.*, 2019, **779**, 784–793.

48 M. Li, H. Li, X. Li, H. Zhu, Z. Xu, L. Liu, J. Ma and M. Zhang, A Bioinspired Alginate-Gum Arabic Hydrogel with Micro-/Nanoscale Structures for Controlled Drug Release in Chronic Wound Healing, *ACS Appl. Mater. Interfaces*, 2017, **9**(27), 22160–22175.

49 S. Ghanavati Nasab, A. Semnani, M. Karimi, M. Javaheran Yazd and S. Cheshmekhezr, Synthesis of Ion-Imprinted Polymer-Decorated SBA-15 as a Selective and Efficient System for the Removal and Extraction of Cu(II) with Focus on Optimization by Response Surface Methodology, *Analyst*, 2019, **144**(15), 4596–4612.

50 H. K. Agbovi and L. D. Wilson, Flocculation Optimization of Orthophosphate with $FeCl_3$ and Alginate Using the Box–Behnken Response Surface Methodology, *Ind. Eng. Chem. Res.*, 2017, **56**(12), 3145–3155.

51 Z. Anfar, R. El Haouti, S. Lhanafi, M. Benafqir, Y. Azougarh and N. El Alem, Treated Digested Residue during Anaerobic Co-Digestion of Agri-Food Organic Waste: Methylene Blue Adsorption, Mechanism and CCD-RSM Design, *J. Environ. Chem. Eng.*, 2017, **5**(6), 5857–5867.

52 H. Mazaheri, M. Ghaedi, M. H. Ahmadi Azqhandi and A. Asfaram, Application of Machine/Statistical Learning, Artificial Intelligence and Statistical Experimental Design for the Modeling and Optimization of Methylene Blue and Cd(II) Removal from a Binary Aqueous Solution by Natural Walnut Carbon, *Phys. Chem. Chem. Phys.*, 2017, **19**(18), 11299–11317.

53 S. Nekouei and F. Nekouei, Comparative Procedure of Photodegradation of Methylene Blue Using N Doped Activated Carbon Loaded with Hollow 3D Flower like ZnS in Two Synergic Phases of Adsorption and Catalytic, *J. Photochem. Photobiol., A*, 2018, **364**, 262–273.

54 N. Minju, G. Jobin, S. Savithri and S. Ananthakumar, Double-Silicate Derived Hybrid Foams for High-Capacity Adsorption of Textile Dye Effluent: Statistical Optimization and Adsorption Studies, *Langmuir*, 2019, **35**(29), 9382–9395.

55 S. Lagergren, About the theory of so-called adsorption of soluble substances, *K. Sven. Vetenskapsakad. Handl.*, 1898, **24**, 1–39.

56 Y. S. Ho and G. McKay, Sorption of Dyes and Copper Ions onto Biosorbents, *Process Biochem.*, 2003, **38**, 1047–1061.

57 X. Ji, G. Kan, X. Jiang, B. Sun, M. Zhu and Y. Sun, A Monodisperse Anionic Silver Nanoparticles Colloid: Its Selective Adsorption and Excellent Plasmon-Induced Photodegradation of Methylene Blue, *J. Colloid Interface Sci.*, 2018, **523**, 98–109.

58 M. F. Abdel Messih, M. A. Ahmed, A. Soltan and S. S. Anis, Synthesis and Characterization of Novel Ag/ZnO Nanoparticles for Photocatalytic Degradation of Methylene Blue under UV and Solar Irradiation, *J. Phys. Chem. Solids*, 2019, **135**, 109086.

59 G. Fan, J. Luo, L. Guo, R. Lin, X. Zheng and S. A. Snyder, Doping Ag/AgCl in Zeolitic Imidazolate Framework-8 (ZIF-8) to Enhance the Performance of Photodegradation of Methylene Blue, *Chemosphere*, 2018, **209**, 44–52.

60 M. A. Ahmed, M. F. A. Messih, E. F. El-Sherbeny, S. F. El-Hafez and A. M. M. Khalifa, Synthesis of Metallic Silver Nanoparticles Decorated Mesoporous SnO_2 for Removal of Methylene Blue Dye by Coupling Adsorption and Photocatalytic Processes, *J. Photochem. Photobiol., A*, 2017, **346**, 77–88.

61 E. A. C. Ferreira, N. F. Andrade Neto, M. R. D. Bomio and F. V. Motta, Influence of Solution PH on Forming Silver Molybdates Obtained by Sonochemical Method and Its Application for Methylene Blue Degradation, *Ceram. Int.*, 2019, **45**(9), 11448–11456.

62 H. A. Rafaie, R. M. Nor, M. S. Azmina, N. I. T. Ramli and R. Mohamed, Decoration of ZnO Microstructures with Ag Nanoparticles Enhanced the Catalytic Photodegradation of Methylene Blue Dye, *J. Environ. Chem. Eng.*, 2017, **5**(4), 3963–3972.

63 Y. Dong, Y. Jiao, B. Jiang and C. Tian, Commercial ZnO and Its Hybrid with Ag Nanoparticles: Photocatalytic Performance and Relationship with Structure, *Chem. Phys. Lett.*, 2017, **679**, 137–145.

64 C. Jaramillo-Páez, J. A. Navío and M. C. Hidalgo, Silver-Modified ZnO Highly UV-Photoactive, *J. Photochem. Photobiol., A*, 2018, **356**, 112–122.

65 B. Sarma and B. K. Sarma, Fabrication of Ag/ZnO Heterostructure and the Role of Surface Coverage of ZnO Microrods by Ag Nanoparticles on the Photophysical and Photocatalytic Properties of the Metal-Semiconductor System, *Appl. Surf. Sci.*, 2017, **410**, 557–565.

66 M. F. Abdel Messih, M. A. Ahmed, A. Soltan and S. S. Anis, Synthesis and Characterization of Novel Ag/ZnO Nanoparticles for Photocatalytic Degradation of Methylene Blue under UV and Solar Irradiation, *J. Phys. Chem. Solids*, 2019, **135**, 109086.

67 N. S. Satdeve, R. P. Ugwekar and B. A. Bhanvase, Ultrasound Assisted Preparation and Characterization of Ag Supported on ZnO Nanoparticles for Visible Light Degradation of Methylene Blue Dye, *J. Mol. Liq.*, 2019, **291**, 111313.

68 M. A. Zeleke and D.-H. Kuo, Synthesis and Application of V_2O_5-CeO_2 Nanocomposite Catalyst for Enhanced Degradation of Methylene Blue under Visible Light Illumination, *Chemosphere*, 2019, **235**, 935–944.